Mechanisms of in-plane shear deformation in hybrid 3D woven composites

R. Muñoz[1], C. González[1,2], J. LLorca[1,2]

[1] *IMDEA Materials Institute, C/ Eric Kandel 2, 28906, Getafe, Madrid, Spain.*
[2] *Department of Materials Science, Polytechnic University of Madrid, E. T. S. de Ingenieros de Caminos. 28040 - Madrid, Spain.*

Abstract

The in-plane shear response of a hybrid 3D woven composite laminate is studied and the deformation and failure micromechanisms are analyzed by means of full-field strain measurements and X-ray microtomography. It was found that the laminate presented a very high failure strain ($\approx 38\%$), much higher than that of conventional 2D laminates, and extensive damage was found to develop during deformation in the form of matrix/fiber debonding and tow splitting by shear. Nevertheless, the through-thickness reinforcement hindered the development of failure by interply delamination and improved the ductility. Final fracture took place by tensile fiber failure and the strain to failure was enhanced by the higher ductility of the glass fibers.

1. Introduction

The mechanical response of fiber-reinforced polymers is controlled either by the fibers when they are deformed in the fiber direction or by the matrix and interface when the dominant deformation is perpendicular to the fibers. In both cases, the strain to failure is of the order of a few percent owing to the limited ductility of fibers and polymeric thermosets. On the contrary, failure under in-plane shear occurs at large strains (above 15%) after significant non-linear deformation [1] . Detailed studies of the deformation and fracture mechanisms of multidirectional laminates in shear X-ray

Email address: javier.llorca@imdea.org (J. LLorca[1,2])

microtomography [2, 3] have shown the complex interaction between matrix, fiber and interface damage during in-plane shear. The linear elastic region is followed by a plateau at which multiple matrix cracks develop parallel to the fibers. Matrix cracking begins by the external plies (due to lower constraint) but it propagates rapidly to the inner plies of the laminate, leading to marked reduction in the shear stiffness. In parallel, the progressive fiber rotation towards the loading axis compensates the reduction in stiffness due to matrix cracking, leading to strain hardening. Final fracture occurs by the development of interply delamination from the matrix cracks in the external plies. Computational micromechanics simulations [4, 5] have validated these results and quantified the role played by the matrix shear strength and the fiber elastic modulus on the shear stress-strain curve of multidirectional laminates. Moreover, they have shown that microstructural factors that facilitate the formation of interply cracks (e.g. weak fiber/matrix interfaces) lead to a marked reduction in the strain-to-failure.

Experimental studies of the in-plane shear deformation of 3D woven composites [6, 7, 8] have shown similar features but the non-linear behavior was more marked and the strain-to-failure was even higher than that of multidirectional laminates. However, a detailed analysis of the micromechanisms of deformation of 3D woven composites in shear has not been carried out yet and thus the role played by the through-the-thickness reinforcement during shear remains unknown. In addition, very little is known about the shear deformation mechanisms of 3D woven composites with hybrid reinforcement and this investigation was aimed at filling these gaps by providing a detailed experimental analysis of the mechanisms of in-plane shear deformation in a 3D hybrid woven composite.

The characterization of the in-plane shear response of a composite is not trivial, particularly in the case of non-symmetric 3D woven laminates. Several experimental techniques were developed to achieve an uniform shear stress in the specimen, including the Iosipescu test [9], the V-notched rail shear test [10] and the tensile shear test [11] (Figure 1). The first two methods provide a quasi-uniform stress state at the ligament between the notches, but special fixtures are needed. The Tensile Shear Test (TST) method provides an uniform shear stress state in the whole specimen and is based on a tensile test in a cross-ply laminate with the layers oriented at [$\pm 45°$] to the loading axis. Unfortunately, the 3D hybrid woven composite studied in this work is not covered by any of these standards because of its non-symmetric structure

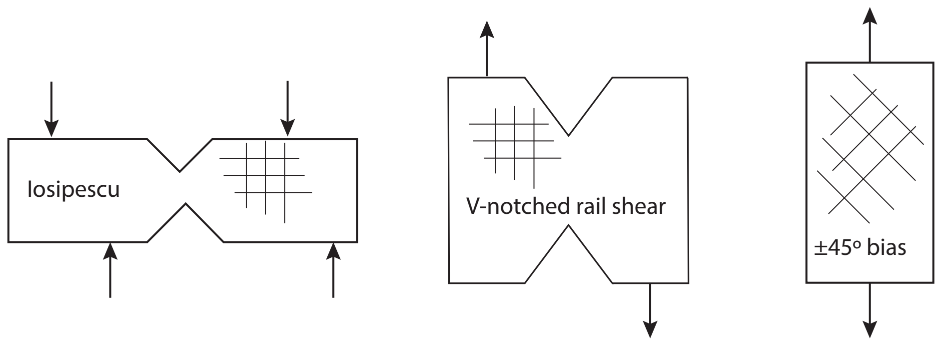

Figure 1: Schematic of experimental techniques to study the in-plane shear behavior of composites. Two notches are machined in the Iosipescu (left) and in the V-notched rail shear (center) specimens, while a tensile test in a cross-ply laminate with the layers oriented at [±45°] to the loading axis is carried out in the Tensile Shear Test Method (right).

and the presence of the binder. However, unlike other preforms (e.g. 3D braided), the 3D fiber preform was orthogonal and did not include fibers inclined to the principal axes, and it can be assumed that the stress state during tensile deformation at [±45°] was similar to that of a standard cross-ply laminate. Thus, the TST was selected to study the shear behavior of the 3D hybrid woven composites. Moreover, the stresses due to the tension-bending coupling because of the non-symmetric structure of the laminate were negligible within the range of validity of the standard [11].

2. Material

A flat composite panel was manufactured by vacuum infusion of an epoxy-vinylester resin (Derakane 8084) into a hybrid 3D orthogonal woven preform. Both the dry perform and the composite panel were provided by 3TEX, Inc. (Cary, North Carolina, USA) with the commercial name p3w-d00001-hx21. The preform was non-symmetric and consisted of three warp (0) and four fill (90) fiber layers stacked as a cross-ply laminate $[90_c,0_c,90_{c/s2},0_{s2},90_{s2},0_{s2},90_{s2}]$, as shown schematically in Figure 2. The fibers in each layer were distributed in tows of rectangular in shape. The four top layers were made up of S2 glass fibers and the two bottom layers of AS4C carbon fibers. The hybrid layer (containing glass and carbon fibers) oriented in the fill direction was located between the glass and the carbon layers. Each tow of this layer contained both AS4C and S2 glass fibers, which were not intermingled but separated in two different zones of the tow (i.e. one half of the tow was formed by

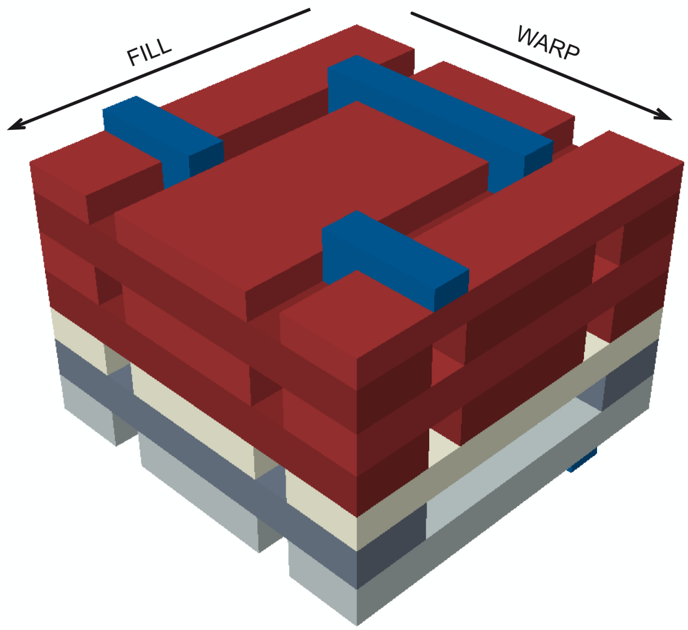

Figure 2: Schematic of the unit cell of the hybrid 3D woven fiber preform. Carbon fiber bundles are shown in grey (dark grey for the warp direction and light grey for the fill), hybrid bundles in white and glass fiber bundles in red (dark red in the warp direction and light red in the fill direction). PE z-yarn binders in the warp direction are plotted in navy blue.

carbon fibers and the other half by glass fibers). In addition, the composite panel was reinforced in the through-thickness direction by z-yarn binders made up of ultra-high molecular weight polyethylene (PE) fibers (Dyneema SK75) that went from top to bottom layers in the warp direction. Note that consecutive z-yarns were in *antiphase*.

The nominal thickness of the dry fabric was 3 mm and its areal density 4.24 Kg/m^2. The nominal thickness of the composite was 4.1 mm, with an areal density of 6.44 Kg/m^2. The overall fiber volume fraction in the composite was 47% and the porosity, as measured by X-ray tomography, was 11.6%. The volume fraction of each type of fiber in each direction (warp or fill) is shown in Table 1. It was determined from the areal density of the individual plies and the fiber density, which were provided by the manufacturer. In addition, the matrix volume fraction (determined from the matrix density and the weight of the composite panel before and after infiltration) is also

Table 1: Density (ρ) and volume fraction of matrix and fibers as a function of fiber type and orientation within the hybrid composite.

Material	ρ (g/cm^3)	warp (%)	fill (%)	total (%)
Glass S2	2.48	15.4	14.7	30.1
Carbon AS4C	1.78	4.3	10.7	15.0
Polyethylene SK75	0.97	1.9	—	1.9
Total fibers		21.6	25.4	47
Matrix	1.02			53

given in Table 1. More details about the material can be found in [12].

3. Experimental Techniques

Four specimens 250 $\times$ 25 $\times$ 4.1 mm^3 were machined with an angle of $\pm 45°$ between the fibers tows and the loading direction. Glass fiber tabs of 50 mm in length were glued to the specimens, leading to a free length of 150 mm (Figure 3). They were tested in tension at room temperature using an electromechanical universal testing machine (Instron 3384) following the recommendations of [11]. Tests were carried out under stroke control at 2 mm/min and the load was continuously measured during the test with a load cell of 150 KN. Both resistive extensometry and Digital Image Correlation (DIC) were used –each in one face of the specimen– to measure the strain along the loading axis, whereas transversal strains were only measured by DIC. This method provides the full displacement field and, unlike strain gages, is not affected by fiber rotation or the roughness of the specimen. DIC was used in the glass face in three specimens and in the carbon face in one specimen. Images obtained with the DIC system were captured every 5 seconds.

The angle θ between fiber tows and the loading direction was measured by optical methods to evaluate the influence of fiber rotation on the mechanical response. This was possible because fiber tows became visible to the naked eye after the matrix was damaged. In addition, one specimen was examined by X-ray computed tomography to ascertain the damage and failure micromechanisms. The region of interest was chosen near the failure section, at the center of the specimen. Measurements were performed with a Nanotom 160NF (Phoenix) at 110kV and 110 mA using a W target. 2300

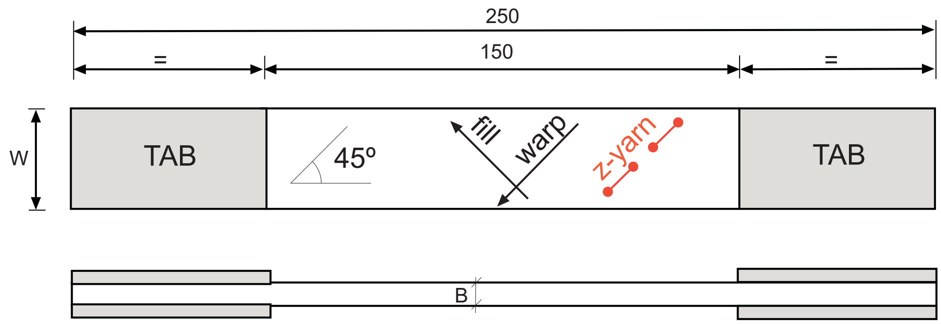

Figure 3: Schematic of the ±45° specimen. Note the directions of the fiber tows and of the z-yarns.

radiographs were acquired for each tomogram with an exposure time of 500 ms. The reconstructed volumes presented a resolution of 11 μm/voxel.

4. Data reduction

The in-plane shear modulus G_{12} and the shear strength S were obtained following the procedure described in the [11]. According to this standard, the in-plane shear stress τ_{12} is given by

$$\tau_{12} = \frac{\mathrm{P}}{2\mathrm{BW}} = \frac{\sigma_x}{2} \tag{1}$$

where P is the applied load, B and W stand for the specimen thickness and width, respectively (Figure 3), and σ_x is the average stress in the loading direction. The shear strain γ_{12} in the coordinate system given by the fiber orientation can be computed as

$$\gamma_{12} = \epsilon_x - \epsilon_y \tag{2}$$

where ϵ_x stands for the longitudinal strain (averaged from the two faces of the specimen) and ϵ_y for the transversal strain in global axes. The in-plane shear modulus G_{12} was computed as the slope of the stress-strain curve between γ_{12}=1.5 10^{-3} and γ_{12}=6.0 10^{-3}. The in-plane shear strength S was the stress at a shear strain of γ_{12} =5 %, as recommended by the standard.

Whilst equations (1) and (2) are valid for small strains, non-linear geometrical effects caused by fiber rotation and net section reduction (necking) cannot be neglected at large deformations. Thus the in-plane shear stress-strain curve was obtained by applying the correction factor K defined by [13]:

$$\tau_{12} = \frac{\sigma_x}{2} K \tag{3}$$

where

$$K = \frac{2Q_{66}(1 + \tan^2\theta)[Q_{12} + Q_{22} + (Q_{11} + Q_{12})\tan^2\theta]\sin 2\theta}{(Q_{12}^2 - Q_{11}Q_{22})(\tan^2\theta - 1)^2 + 4(Q_{11} + 2Q_{12} + Q_{22})Q_{66}\tan^2\theta} \tag{4}$$

where Q_{ij} are the components of the stiffness matrix of each ply, and θ the angle between the loading direction and the tows. Since this laminate contains dissimilar materials, K was approximated by $\overline{K}$, which is given by

$$\overline{K} = \sum_{i=1}^{n} K^i V_f^i \tag{5}$$

where V_f^i and K^i are, respectively, the volume fraction and the correction factor of each ply i, and n is the total number of layers.

Likewise, the shear strain γ_{12} is expressed by

$$\gamma_{12} = -(\varepsilon_x - \varepsilon_y)\sin 2\theta + \gamma_{xy}\cos 2\theta \tag{6}$$

where the global shear strain γ_{xy} was neglected. Assuming that fibers are free to rotate, the angle θ can be approximated by

$$\theta = \arctan\left[\frac{\pi}{4}\frac{1 - \epsilon_y}{1 + \epsilon_x}\right] \tag{7}$$

and the accuracy of this expression was validated by the experimental results in Fig. 4

Net section reduction (necking) was not negligible, so it was also accounted for. The current transverse section A can be expressed as a function of the initial section A_0 as $A = A_0(1 - \epsilon_x)$.

5. Results and discussion

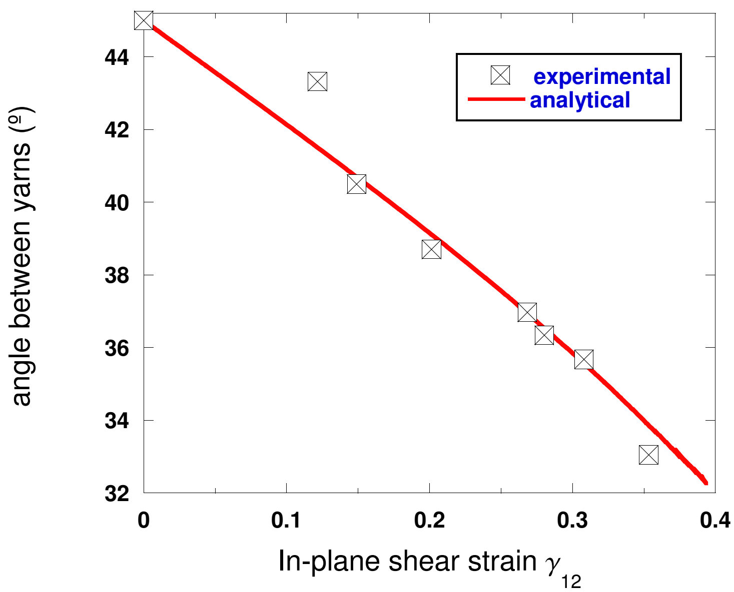

Figure 4: Evolution of angle between yarns and the loading direction, θ, as a function of the applied shear strain γ_{12}.

Table 2: In-plane shear properties of the hybrid 3D woven composite

G_{12} (GPa)	S (MPa)
3.4 ± 0.9	27.3 ± 2.0

Two shear stress-strain curves are plotted in Figure 5. They were very similar, indicating that the size of the coupons was large enough to capture the effective behavior of the composite. The average values and the standard deviation of the shear modulus, G_{12}, and of the shear strength, S, are shown in Table 2. The material presented an initial elastic region up to $\gamma_{12} \approx 1\%$, which was followed by a region of non-linear deformation up to $\approx 15\%$ in which the composite presented strain hardening. Afterwards, the stress carried out by the composite remained more or less constant and final fracture occurred at an applied shear strain close to 40%. It should be noted that the shear stiffness and strength were much lower than those usually found 2D laminates although the strain to failure was much higher. The low stiffness and strength can be attributed to the porosity in the matrix and to the limited bonding between the matrix and the fiber yarns.

The contour plot of the shear strain on the specimen surface obtained by DIC showed that the longitudinal strain, ε_x, was localized in shear bands parallel to the fibers from the onset of the non-linear regime (Figure 5). In addition, optical micrographs at different strains showed the development of matrix cracks parallel to the fibers and perpendicular the loading axis in the non-linear deformation regime. The crack density increased with the applied strain, as it can be seen in the specimen prior to the final failure (Figure 6). It is worth noting that load carrying capability of the composite increased with strain up to 15% and remained more or less constant afterwards until failure in the presence of extensive matrix cracking and this was due to the strengthening provided by fiber rotation, which compensate the stiffness degradation induced by matrix cracking [2].

The inspection by X-ray computed tomography of the broken specimen provided more information about the deformation and damage mechanisms that developed upon non-linear deformation at the ply and laminate level. Within each ply, the kinematic incompatibility between the matrix and the fiber tows led to the development of in-plane shear stresses parallel to the yarns. They induced extensive yarn/matrix debonding (facilitated by the

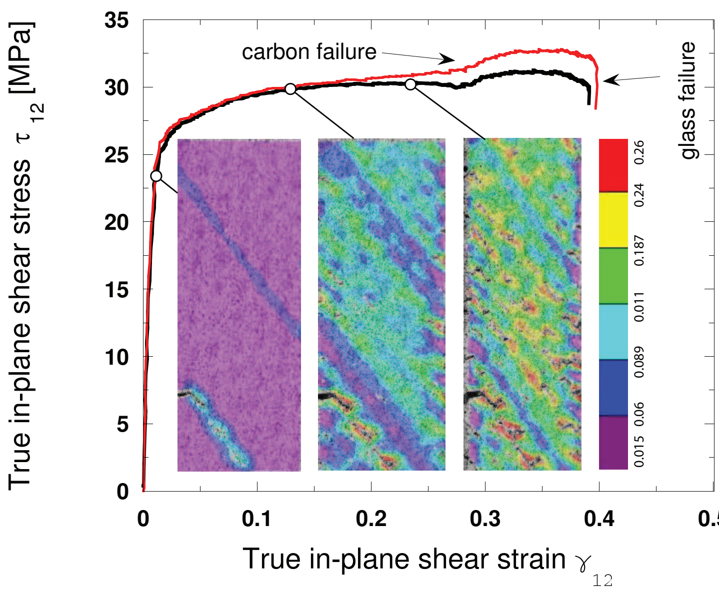

Figure 5: In-plane shear stress *vs* shear strain curves of the hybrid 3D woven composite. The contour plots of the Green-Lagrange longitudinal strain on the specimen surface obtained by DIC are shown for different applied strains.

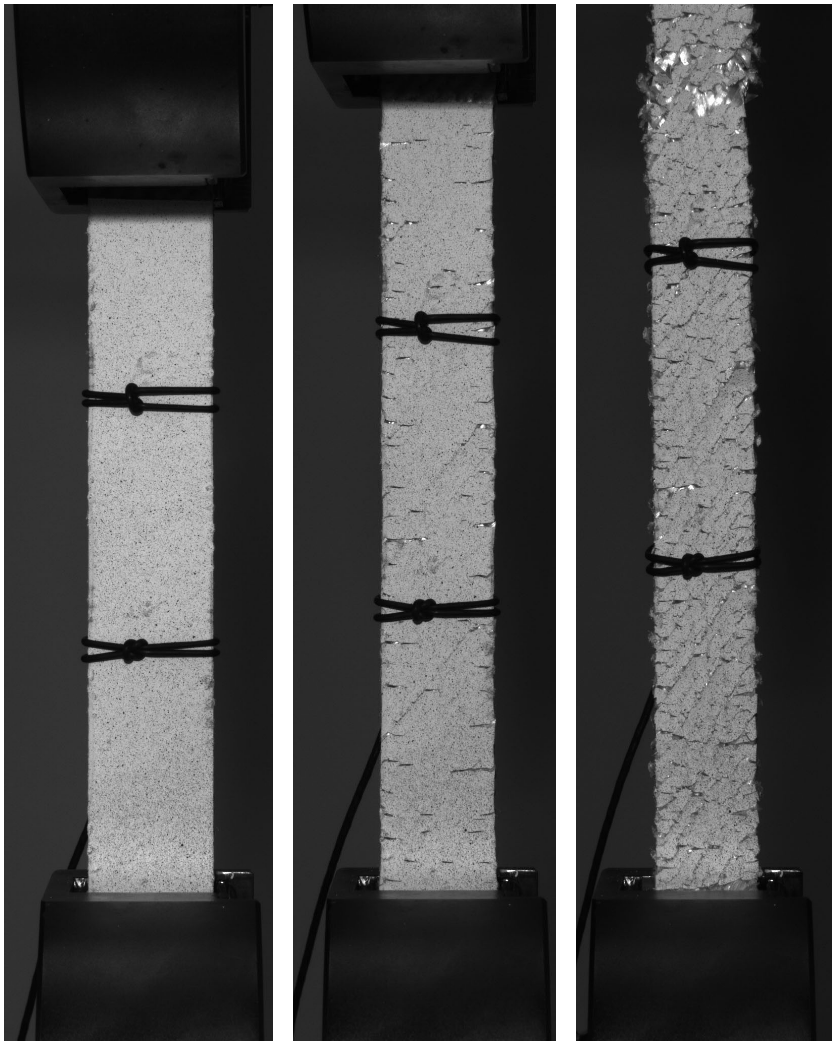

(a) $\gamma_{12} = 0$

(b) $\gamma_{12} = 18\%$

(c) $\gamma_{12} = 38\%$, close to final failure

Figure 6: Optical micrographs showing the development of cracks parallel to the fibers and perpendicular to the loading axis as a function of the applied strain.

poor bonding between them) as well as tow splitting (Figure 7). The cross-sections of the laminate perpendicular to the warp and fill yarns showed that tow splitting by shear cracks as well as matrix debonding from either fiber tows or z-yarns were the dominant damage mechanisms during deformation (Figure 8). It is worth noting that shear cracks within the fiber tows were inclined with respect to the vertical direction (Figure 8). This is likely due to the crimping induced by the binder in the carbon fill yarns which cause a non-uniform distribution of the frictional forces acting along the tow.

At laminate level, the z-yarns were able to hold together the laminate during deformation and hindered the early fracture by the propagation of interply cracks. In addition, large deformations induced the rotation of the fibers in different plies in opposite directions, giving rise to the so-called *scissoring effect* in which the interface between plies oriented at $\pm$ 45° is subjected to in-plane shear forces. As depicted in Figure 9, this rotation causes shear cracking at the matrix ligaments between two consecutive z-yarns as well as extensive yarn-matrix debonding. In unidirectional composites this effect is only constrained by the matrix between layers, leading to delamination. The rotation of the fill yarns is, however, constrained by the friction with the z-yarns in 3D woven composites. This causes a stress concentration that leads to extensive z-yarn-matrix debonding (Figures 7 and 9).

The final fracture of the 3D woven laminate was not due to interply delamination and has to be attributed to tensile fracture of the fibers. In fact, the evolution of the longitudinal strain in the fiber tows with the applied strain, ϵ_1, can be computed as a function of the longitudinal (ϵ_x) and transverse (ϵ_y) applied to the laminate (Fig. 10) according to

$$\epsilon_1 = \frac{l_f}{l_i} - 1 \tag{8}$$

where l_f and l_i stand for the final and initial tow length, respectively, which can be expressed by simple geometrical considerations as,

$$l_i = \sqrt{2}W \quad \text{and} \quad l_f = \sqrt{(W-\Delta_y)^2 + (W+\Delta_x)^2} \tag{9}$$

with

$$\Delta_y = \varepsilon_y W, \quad \Delta_x = \varepsilon_x W \tag{10}$$

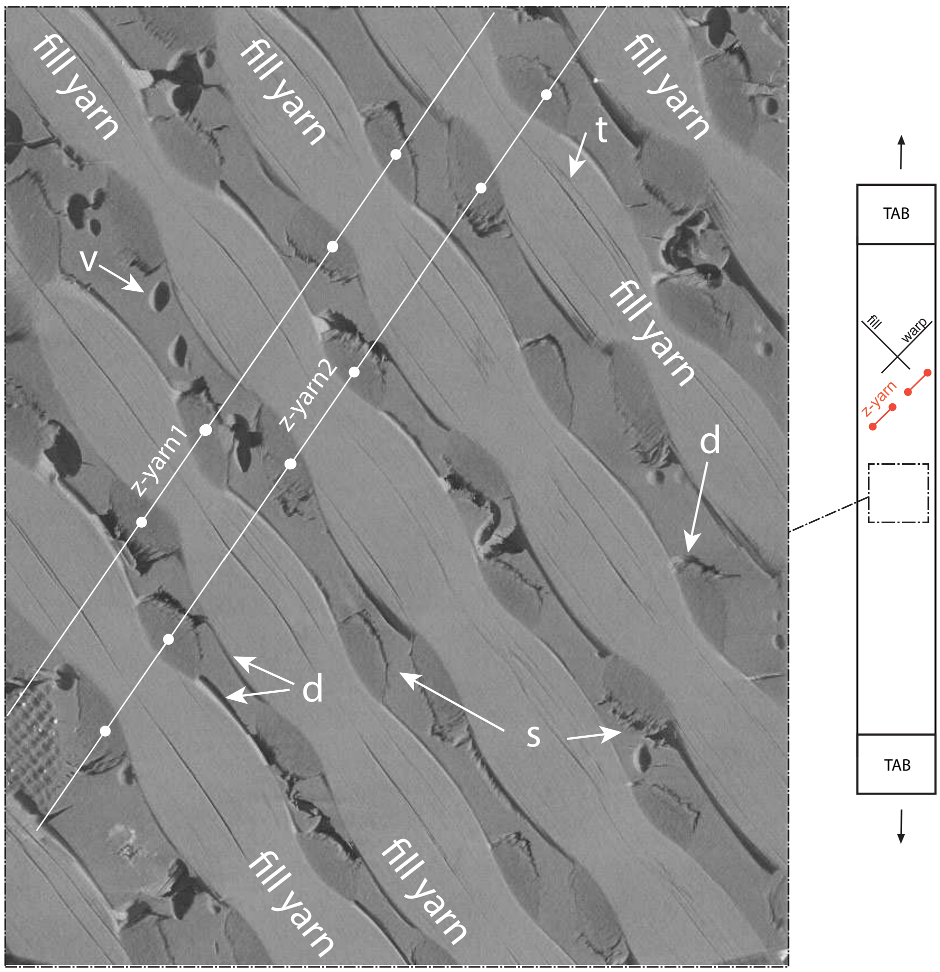

Figure 7: Section parallel to the laminate surface across the carbon fill ply. Carbon fiber tows and matrix appear light grey. The orientation of two adjacent z-yarns (z-yarn1 and z-yarn2) is indicated with two parallel white lines. White filled dots indicate the location of the corresponding z-yarn cross sections. Arrows indicate the different damage mechanisms: d stands for matrix debonding from the carbon fiber tows or the z-yarns, t tow splitting within the fiber tows and s shear cracks at matrix ligaments constrained by two consecutive z-yarns. v indicates voids.

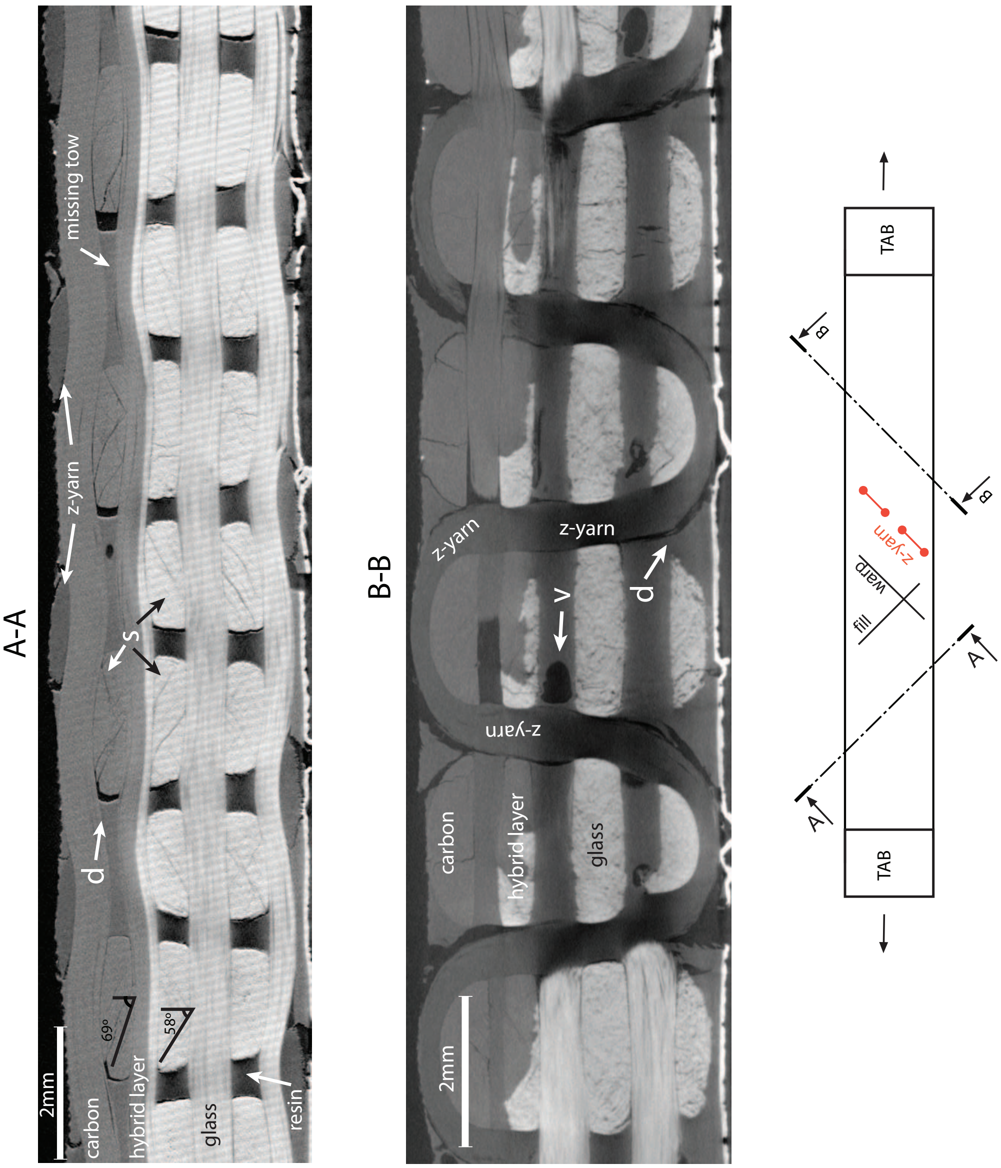

Figure 8: Cross section perpendicular to the warp tows and z-yarns (A-A) and cross section perpendicular to the fill tows (B-B). Glass fiber tows appear light grey, carbon fiber tows appear dark grey, z-yarn and the matrix appear slightly darker than carbon yarns and the white region at the bottom corresponds to DIC speckle pattern. Arrows indicate the different damage mechanisms: v stands for voids, d for matrix debonding from the fiber tows or the z-yarns and s indicates shear cracking within the tow. The shear cracks within glass and carbon tows were oriented at $\approx 58°$ and $\approx 69°$, with respect to the through-thickness direction, respectively.

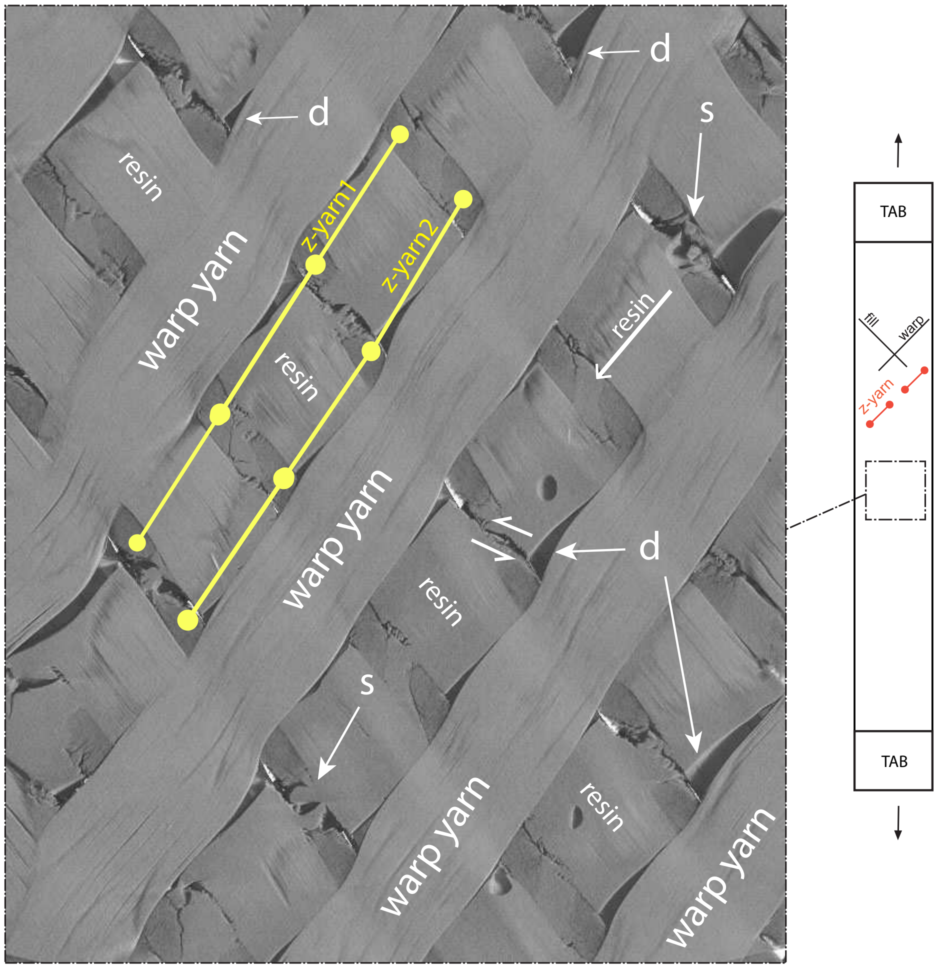

Figure 9: Section parallel to the laminate surface containing the carbon warp ply. Carbon fiber yarns and the matrix appear light grey. The orientation of two adjacent z-yarns (z-yarn1 and z-yarn2) is indicated with two parallel yellow lines. Yellow filled dots indicate the location of the corresponding z-yarn cross sections, which appear dark grey. Arrows indicate the different damage mechanisms: *d* stands for delamination of the fiber tows or the z-yarns, *s* for shear cracks at matrix ligaments constrained by two consecutive z-yarns. Extensive shear cracking is visible at the matrix ligaments located between z-yarns. Yarn-matrix debonding is also clearly depicted.

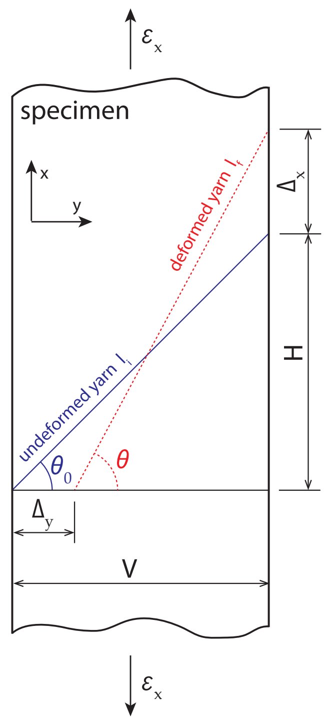

Figure 10: Schematic of the calculation of the longitudinal strain in the fiber tows in local coordinates as a function of the applied strain. The continuous blue line stands for a tow in the undeformed configuration, and the dotted red line is a tow in the deformed configuration.

where $W = 25$ mm. The evolution of the longitudinal fiber strain with the applied shear strain is plotted in Fig. 11. This curve shows that the slight load reduction at $\gamma_{12} = 2.9\%$ corresponds to a longitudinal strain in the fiber direction of $\approx 1.4\%$, which is very close to the failure strain of the AS4C carbon fiber towss ($1.5 \pm 0.2\%$) [12]. The longitudinal strain in the fiber direction at failure was $\approx 2.2\%$, which is smaller than the tensile failure strain of the S2 glass fiber tows ($4.0 \pm 1.0\%$) [12]. Nevertheless, the failure strain of the 3D woven composite in tension along the fill direction was also in the range 2.0 to 2.5% and it was triggered by the failure of the glass fibers after the premature failure of the carbon fiber tows at smaller strains. The early fracture of the S2 glass fiber tows in tension was attributed to the bending stresses induced in the non-symmetric hybrid laminate after the failure of the carbon fibers and to the stress concentration in the vicinity of failed tows [12]. These mechanisms can also be operative under in-plane shear deformation and are responsible for the large failure strain of 3D woven composites in shear, which is controlled by the tensile failure of the glass fibers. This is in contrast with the behavior of 2D laminates, in which interply delamination leads to failure at lower strains (15-20%) [1, 5, 2]

6. Conclusions

The in-plane shear deformation as well as the associated failure micromechanisms were studied in a 3D hybrid woven composites. The composite presented a very large ductility (failure strains of $\approx 38\%$) and extensive ply damage in the form of debonding of the matrix from the fiber tows and z-yarns together with tow splitting by shear. Nevertheless, the presence of the z-yarns in the through-thickness direction impeded the propagation of damage along the interplies and interply delamination did not develop, enhancing the ductility of the laminate as compared with 2D materials. Progressive rotation of the fibers along the loading direction led to the final fracture by the tensile fracture of the glass fibers, whose presence enhanced the strain to failure of the composite.

Acknowledgements This investigation was supported by the Spanish Ministry of Economy and Competitiveness through the project MUDATCOM (MAT2012-37552). The authors acknowledge 3TEX Inc. for providing the material and the areal densities.

[1] W. Van Paepegem, I. De Baere, J. Degrieck, Modelling the nonlinear shear stress-strain response of glass fibre-reinforced composites. Part I:

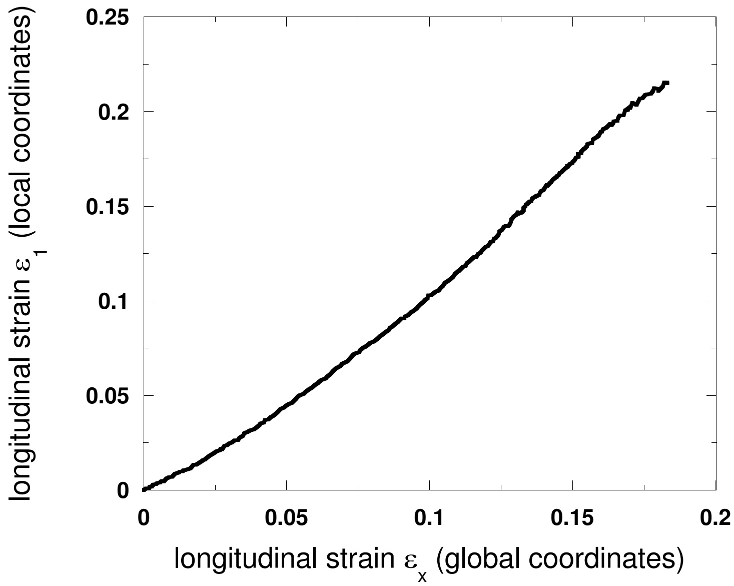

Figure 11: Evolution of the longitudinal strain in the fiber tows as a function of the applied shear strain, γ_{12}.

Experimental results, Composites Science and Technology 66 (10) (2006) 1455–1464.

[2] F. Sket, A. Enfedaque, C. Alton, C. González, J. Molina-Aldareguia, J. Llorca, Automatic quantification of matrix cracking and fiber rotation by X-ray computed tomography in shear-deformed carbon fiber-reinforced laminates, Composites Science and Technology 90 (2014) 129–138.

[3] F. Sket, M. Rodríguez-Hortalá, J. M. Molina-Aldareguía, J. LLorca, E. Maire, G. Requena, Tomographic investigation of damage development during tensile loading of ±45° carbon fibre reinforced laminates, Materials Science and Technology (2014) in press.

[4] E. Totry, C. González, J. LLorca, J. M. Molina-Aldareguía, Mechanisms of shear deformation in fiber-reinforced polymers: Experiments and simulations, International Journal of Fracture 158 (2009) 197–209.

[5] E. Totry, J. M. Molina-Aldareguía, C. González, J. LLorca, Effect of

fiber, matrix and interface properties on the in-plane shear deformation of carbon-fiber reinforced composites, Composites Science and Technology 70 (2010) 970–980.

[6] A. E. Bogdanovich, M. Karahan, S. V. Lomov, I. Verpoest, Quasi-static tensile behavior and damage of carbon/epoxy composite reinforced with 3D non-crimp orthogonal woven fabric, Composites Science and Technology 62 (0) (2013) 14–31.

[7] R. Gerlach, C. R. Siviour, J. Wiegand, N. Petrinic, In-plane and through-thickness properties, failure modes, damage and delamination in 3D woven carbon fibre composites subjected to impact loading, Composites Science and Technology 72 (3) (2012) 397–411.

[8] S. V. Lomov, A. E. Bogdanovich, D. S. Ivanov, D. Mungalov, M. Karahan, I. Verpoest, A comparative study of tensile properties of non-crimp 3D orthogonal weave and multi-layer plain weave E-glass composites. Part 1: Materials, methods and principal results, Composites Part A: Applied Science and Manufacturing 40 (8) (2009) 1134–1143.

[9] ASTM D5379, Standard test method for in-plane shear properties of composite materials by the V-notched beam method (2001).

[10] ASTM D7078, Standard test method for shear properties of composite materials by the V-notched rail shear method (1995).

[11] ASTM D3518, Standard Test Method for In-Plane Shear Response of Polymer Matrix Composite Materials by Tensile Test of a 45 Laminate.

[12] R. Muñoz, V. Martínez, F. Sket, C. González, J. Llorca, Mechanical behavior and failure micromechanisms of hybrid 3D woven composites in tension, COMPOSITES PART A 59 (2014) 93–104.

[13] M. Wisnom, The effect of fibre rotation in 45 tension tests on measured shear properties, Composites 26 (1) (1995) 25–32.